

# Approximating the particle distribution in rotating and tandem mirror traps

G.X. Li<sup>1</sup> , E.J. Kolmes<sup>2</sup> , I.E. Ochs<sup>2</sup>  and N.J. Fisch<sup>2</sup> 

<sup>1</sup>Department of Physics, Princeton University, Princeton, NJ 08544, USA

<sup>2</sup>Department of Astrophysical Sciences, Princeton University, Princeton, NJ 08544, USA

Corresponding author: G.X. Li, [greta.li@princeton.edu](mailto:greta.li@princeton.edu)

(Received 27 May 2025; revision received 24 July 2025; accepted 10 August 2025)

Steady-state distribution functions can be used to calculate stability conditions for modes, radiation energy losses and particle loss rates. Heuristic analytic approximations to these distributions can capture key behaviors of the true distributions such as the relative speeds of different transport processes while possessing computational advantages over their numerical counterparts. In this paper, we motivate and present a closed-form analytic model for a distribution of particles in a centrifugal or tandem mirror. We find that our model outperforms other known models in approximating numerical steady-state simulations outside of a narrow range of low confining potentials. We demonstrate the model's suitability in the high confining potential regime for applications such as loss-cone stability thresholds, fusion yields and available energy.

**Key words:** plasma instabilities, fusion plasma

## 1. Introduction

There has been growing interest in open field line configurations for magnetic plasma confinement. This includes conventional mirrors, centrifugal mirrors and tandem mirrors. In centrifugal traps with electric field  $\mathbf{E}$  and magnetic field  $\mathbf{B}$ , rotation is induced by an  $\mathbf{E} \times \mathbf{B}$  drift, which introduces a centrifugal potential that improves plasma confinement (Lehnert 1971; Bekhtenev *et al.* 1980; Ellis *et al.* 2001; Teodorescu *et al.* 2010) and can improve plasma stability (Bekhtenev *et al.* 1980; Abdrashitov *et al.* 1991; White, Hassam & Brizard 2018; Kolmes, Ochs & Fisch 2024). For tandem mirrors, end plugs generate a confining potential in the center cell. Magnetic mirrors possess practical advantages over other confinement configurations that are important to consider in the path to commercial fusion. In particular, the open-ended axial magnetic system of mirrors is relatively simpler to build and maintain than the closed toroidal systems of tokamaks and stellarators, and mirror systems can contain plasmas with high beta, or ratio of plasma pressure to magnetic pressure, in steady-state operation (Post 1987).

Advancements in mirror technology, as demonstrated in GAMMA-10 (Cho *et al.* 2005), the Maryland Centrifugal Mirror eXperiment (Ellis *et al.* 2005) and the gas dynamic trap (Ivanov & Prikhodko 2013, 2017), have paved the path for further

mirror development with experiments such as the Wisconsin HTS Axisymmetric Mirror (Egedal *et al.* 2022), the Centrifugal Mirror Fusion eXperiment (White *et al.* 2018), the SMOLA device (Sudnikov *et al.* 2017) and multiple mirror traps (Be'ery *et al.* 2018; Miller *et al.* 2021).

Apart from its use in fusion, centrifugal mirror confinement is effective in differential containment devices, namely devices used for mass separation (Hidekuma *et al.* 1974; Hiroe *et al.* 1975; Weibel 1980; Ohkawa & Miller 2002; Litvak *et al.* 2003; Fetterman & Fisch 2011; Gueroult & Fisch 2014; Gueroult, Rax & Fisch 2014; Timofeev 2014; Gueroult *et al.* 2015; Vorona *et al.* 2015; Dolgolenko & Muromkin 2017; Gueroult *et al.* 2018; Oiler *et al.* 2024). The regime of large plasma rotation in centrifugal mirror devices is where differentiating particles on the basis of mass is particularly effective. It also happens to be the regime of the greatest pertinence here.

In the literature on standard (non-centrifugal) mirrors, studies have heavily relied on heuristic approximations to the steady-state particle distribution in phase space (Rosenbluth & Post 1965; Post & Rosenbluth 1966; Futch *et al.* 1972; Tang, Pearlstein & Berk 1972; Newcomb 1981; Smith 1984; Smith, Nevins & Sharp 1984). This approach has been particularly productive for calculations of stability conditions for loss-cone modes. However, despite the important role played by kinetic physics in the centrifugal or tandem traps, the corresponding approximations are far less well developed in the literature on mirror traps with an arbitrary confining potential.

Previous approaches to capturing rotating loss-cone behavior include applying prefactors that vanish at the loss-cone boundary (Volosov, Pal'chikov & Tsel'nik 1969; Turikov 1973; Khudik 1997), modifying a Maxwellian distribution to suppress values in the loss cone (Catto & Li 1985; Kolmes *et al.* 2024; Kolmes & Fisch 2024) and leveraging other known distributions with some loss-cone features and thermal anisotropy (Summers & Stone 2025).

The purpose of this paper is to consider how best to construct a heuristic approximation for the distribution of particles in a low-collisionality rotating or tandem mirror. We propose a new analytic closed-form model that improves upon past models and reflects the relative dominance of pitch angle scattering compared with energy scattering. We also examine how different heuristic approximations perform in different contexts and how best to understand the suitability of a given approximation for a given application.

The paper is structured as follows. Section 2 reviews previous models which motivate the general form of the class of solutions that we consider in Section 3. Section 4 covers the numerical scheme from Ochs, Munirov & Fisch (2023) that we use to validate our model. Section 5 presents our analytic approximation explicitly and a useful parametrization of space. Section 6 analyzes the error of our model compared with numerical simulations, finding that our model outperforms other known models in the regime where the confining potential  $\phi \gtrsim 2$ . Section 7 examines the suitability of the model in three applications: loss-cone stability thresholds, fusion yields and free energy. To conclude, Section 8 discusses the suitability and potential adjustments of our model for different confinement regimes.

## 2. Prior models

The distribution of particles in a centrifugal or tandem trap is typically not Maxwellian. Rather, these traps have loss cones: regions of phase space in which particles are not confined. It is constructive to explicitly review parameters and equations relevant to plasmas in magnetic mirrors with an arbitrary confining potential.

We then examine previous proposed models before reducing our search to functions of a certain form.

Suppose we have a mirror machine with magnetic field strength  $B$ , which is greatest at the ends and smallest at the mid-plane, and confining potential  $\phi$ , which could include the electrostatic potential and centrifugal potential due to rotation (Post 1987). We define the mirror ratio  $R_0$  as

$$R_0 := \frac{B_{\text{end}}}{B_{\text{mid}}}, \quad (2.1)$$

where  $B_{\text{end}}$  and  $B_{\text{mid}}$  are the magnetic fields evaluated at the mirror ends and mid-plane, respectively. We also define a dimensionless difference of confining potential evaluated at the ends and the mid-plane

$$\phi := \frac{\varphi_{\text{end}} - \varphi_{\text{mid}}}{T}. \quad (2.2)$$

Here,  $\varphi_{\text{end}}$  and  $\varphi_{\text{mid}}$  are the respective potentials at the ends and at mid-plane of the device, including both centrifugal and electrostatic components, and  $T$  is the plasma temperature.

Assuming that the first adiabatic invariant, the magnetic moment, is conserved, we can derive the confinement condition from Post (1987)

$$0 \leq \phi + R_0 x^2 \sin^2(\theta) - x^2, \quad (2.3)$$

where  $x$  is the dimensionless speed of the particle (normalized to the thermal speed) and  $\theta$  is the pitch angle, which is the angle between the direction of the velocity and the direction of the magnetic field.

The loss-cone region of momentum space contains all the points  $(x, \theta)$  such that the above inequality does not hold. Any particles that diffuse into the loss-cone region are lost from the system. Increasing either the mirror ratio  $R_0$  or the generic confining potential  $\phi$  will shrink the loss-cone region, thus improving the confinement of the system.

We briefly review prior proposed models. One such analytic model is the truncated Maxwellian, which is the Maxwellian distribution function with values in the loss cone sent to zero, as used in Kolmes *et al.* (2024)

$$f_{\text{tm}}(x, \theta) = A [\pi^{-3/2} e^{-x^2}] \Theta(\phi + R_0 x^2 \sin^2(\theta) - x^2), \quad (2.4)$$

where  $A$  is the normalization constant such that the integral of the momentum-space distribution over all space evaluates to unity and  $\Theta$  is the Heaviside step function that cuts out the loss-cone region.

This model has the advantage in its relative simplicity and recovery of the Maxwellian distribution in the limit as  $\phi \rightarrow \infty$ . The loss-cone vertex is located at  $(\sqrt{\phi}, 0)$ , so in this limit, the loss-cone region shifts far away from the bulk of the particle distribution. However,  $f_{\text{tm}}$  has distinctly un-physical behavior at the loss-cone boundary due to the infinite gradient there. This becomes an issue for applications like fusion yield calculations in cases where the confining potential is not large.

For the steady-state distribution  $f$  solution to the linearized Fokker–Planck equation, Najmabadi, Conn & Cohen (1984) find an analytic prefactor  $g := f/f_M$ , where  $f_M$  is the Maxwellian and  $g$  has adjustable parameters

$$g(x, \theta) = 1 - q_0 \ln \left( \frac{e^{a^2} + e^{x^2} + \sqrt{\rho^2 + (e^{a^2} + e^{x^2})^2}}{e^{a^2} - e^{x^2} + \sqrt{\rho^2 + (e^{a^2} - e^{x^2})^2}} \right), \quad (2.5)$$

where

$$\begin{aligned} q_0 &:= \left( \ln \left( \frac{w+1}{w-1} \right) \right)^{-1} & w &:= \left( 1 + \frac{1}{Z_{\perp,s} R_0} \right)^{1/2} \\ a &:= (\ln(w) + \phi)^{1/2} & \rho &:= \left( \frac{2x^2}{Z_{\perp,s}} \right)^{1/2} e^{x^2} \tan(\theta). \end{aligned} \quad (2.6)$$

The species-dependent constant  $Z_{\perp}$  is defined as the following for ion species  $a$  and electron species  $e$ :

$$Z_{\perp,a} := \frac{1}{2} \left( \frac{\sum_b n_b Z_b^2 \lambda_{ab}}{\sum_b n_b Z_b^2 \lambda_{ab} m_a T_b / m_b T_a} \right), \quad (2.7a)$$

$$Z_{\perp,e} := \frac{1}{2} \left( 1 + \frac{\sum_b n_b Z_b^2 \lambda_{eb}}{n_e \lambda_{ee}} \right), \quad (2.7b)$$

where  $Z_b$ ,  $m_b$ ,  $n_b$ ,  $T_b$  are the charge, mass, density and temperature of other species  $b$ , respectively, and  $\lambda_{ab}$  is the Coulomb logarithm. Faster species are excluded from the sums.

We removed the correction term  $1/4x^2$  in  $\rho$  and  $w$  to avoid divergence at the origin. This formulation does not go to zero at the loss-cone boundary, but for the sake of later comparison, we apply a Heaviside step function  $\Theta$  that cuts out the loss-cone region and then re-normalize the distribution. One advantage of this model is the explicit dependence on  $Z_{\perp}$ . However, in order to calculate the collisional end loss rates, the focus is on approximating the region within one e-folding of the loss-cone vertex. We will see later that this leads to a weaker approximation for the bulk of the distribution if the vertex is sufficiently far away from the origin.

An earlier analytic model used by Volosov *et al.* (1969) and Turikov (1973) is as follows:

$$f_{\text{vol}}(x, \theta) = A \left[ \sqrt{\phi + R_0 x^2 \sin^2(\theta) - x^2 e^{-x^2 \sin^2(\theta)}} \right] \Theta(\phi + R_0 x^2 \sin^2(\theta) - x^2), \quad (2.8)$$

where  $A$  is the normalization constant. When  $\phi = 0$  and  $R_0 = 2$ ,  $f_{\text{vol}}$  reduces to the analytic model of a standard non-rotating mirror in Rosenbluth & Post (1965). The prefactor term in the square root ensures that the model smoothly decays to zero at the loss cone. However, in the limit as  $\phi \rightarrow \infty$ , the analytic model does not recover the Maxwellian distribution due to the exponential term's dependence on only the perpendicular component of momentum,  $x \sin(\theta)$ .

More recently, subtracted-kappa distributions have been suggested to approximate loss-cone-like regions for space plasmas by Summers & Stone (2025), particularly in contexts where anisotropy is important. However, we will restrict our scope here to models that vanish within the loss cone described by (2.3).

Trial functions  $h := f/f_M$  have also been used to find particle loss rates in mirrors, where  $h$  serves as a prefactor to the Maxwellian distribution  $f_M$  (Catto & Bernstein 1981; Catto & Li 1985; Khudik 1997). In particular, an iso-contours approach is used where lines of constant  $h$  can be used in their integral calculations. However, although their application did not require or provide an explicit analytic expression for  $h$ , we find this approach informative and will pursue it further.



### 3. Function properties

It is convenient to write candidate models as the product of a truncated Maxwellian and some prefactor function. Note, only the restrictions on the prefactor itself limit the class of allowable functions for the distribution function. Let our model be  $f_{\text{mod}}$  and prefactor be  $g_{\text{mod}}$

$$f_{\text{mod}}(x, \theta; R_0, \phi) = A \left[ g_{\text{mod}}(x, \theta; R_0, \phi) \left( \pi^{-3/2} e^{-x^2} \right) \right] \Theta(\phi + R_0 x^2 \sin^2(\theta) - x^2), \quad (3.1)$$

where  $R_0$  and  $\phi$  are included as parameters to emphasize the model's dependency on them. We provide the explicit normalization constant

$$A = \left( \int dx d\theta \, 2\pi x^2 \sin(\theta) \left[ g_{\text{mod}} f_{\text{tm}} \right] \right)^{-1}, \quad (3.2)$$

where the  $2\pi$  comes from the distribution's cylindrical symmetry in momentum-space after assuming gyrotropy and  $f_{\text{tm}}$  is the truncated Maxwellian model. Our prefactor  $g_{\text{mod}}$  is of the following form,

$$g_{\text{mod}}(x, \theta; R_0, \phi) = \frac{f_{\text{mod}}(x, \theta; R_0, \phi)}{f_{\text{tm}}(x, \theta; R_0, \phi)} \quad (3.3)$$

up to the normalization constant. For example, the normalized truncated Maxwellian would correspond to the constant prefactor

$$g_{\text{tm}}(x, \theta; R_0, \phi) = 1. \quad (3.4)$$

Instead of directly analytically approximating  $f_{\text{mod}}$  to some numerical steady-state distribution  $f_{\text{sim}}$ , we can instead fit the prefactor  $g_{\text{mod}}$  to a weighted simulation, which is defined as  $g_{\text{sim}} := f_{\text{sim}}/f_{\text{tm}}$ . This quantity measures how similar the simulation value is to the truncated Maxwellian value at a point. We will require our prefactor to force a smooth decay to zero at the loss cone while having negligible effect on the truncated Maxwellian in the limit as  $\phi \rightarrow \infty$ .

Furthermore, our mirror system has cylindrical symmetry due to the lack of azimuthal angle dependency. This symmetry forces us to consider a prefactor such that

$$\left. \frac{\partial g_{\text{mod}}}{\partial \theta} \right|_{\theta=\pi/2} = 0, \quad (3.5)$$

where  $\theta = \pi/2$  corresponds to the plane of momentum phase space for particles with velocities perpendicular to the magnetic field.

### 4. Simulation set-up

In order to validate different features of these heuristic models, we use Fokker–Planck simulations. Here, we review those simulations. Namely, we explain relevant parameters and coordinates as well as choice of source, temperature and species. Furthermore, we expand on desired properties for the prefactor  $g_{\text{mod}}$  that are tailored to our numerical simulation's domain.

To obtain a numerical steady-state particle distribution  $f_{\text{sim}}$  of a magnetic mirror, we simulate the collisional process governed by the Fokker–Planck diffusion

equation for an arbitrary species  $a$  (Najmabadi *et al.* 1984; Ochs *et al.* 2023; Rosen *et al.* 2025)

$$\tau_{0,a} \frac{\partial f_a}{\partial t} = \frac{1}{x^2} \frac{\partial}{\partial x} \left( Z_{\parallel,a} f_a + \frac{1}{2x} \frac{\partial f_a}{\partial x} \right) + \frac{1}{x^3} \left( Z_{\perp,a} - \frac{1}{4x^2} \right) \frac{\partial}{\partial \xi} \left[ (1 - \xi^2) \frac{\partial f_a}{\partial \xi} \right], \quad (4.1)$$

where we have followed the convention in broader mirror literature by assuming gyrotropy and using the following dimension-less coordinates:

$$x = \frac{v}{v_{th,a}}, \quad \xi = \frac{v_{\parallel}}{v}, \quad v_{th,a} := \sqrt{2T_a/m_a}. \quad (4.2)$$

Here,  $v_{th,a}$  is the thermal speed,  $v_{\parallel}$  is the component of the velocity parallel to the magnetic field,  $m_a$  is the particle mass and  $\tau_{0,a}$  is the collision time of species  $a$ . Intra-species collisions are included.

The coordinate-transformed diffusion equation contains two species-dependent quantities,  $Z_{\parallel,a}$  and  $Z_{\perp,a}$ ,

$$Z_{\parallel,a} := \frac{\sum_b n_b Z_b^2 \lambda_{ab} / m_b}{\sum_b n_b Z_b^2 \lambda_{ab} T_b / m_b T_a}, \quad Z_{\perp,a} := \frac{1}{2} \frac{\sum_b n_b Z_b^2 \lambda_{ab}}{\sum_b n_b Z_b^2 \lambda_{ab} m_a T_b / m_b T_a}, \quad (4.3)$$

where  $Z_b$ ,  $m_b$ ,  $n_b$ ,  $T_b$  are the charge, mass, density and temperature of other species  $b$ , respectively,  $\lambda_{ab}$  is the Coulomb logarithm and  $Z_{\perp,a}$  was defined above in (2.7) as the constant for an ion species. Since the electron species expression,  $Z_{\perp,e}$ , is consistent with the ion species expression after ignoring ion–electron collisions, we redefine  $Z_{\perp,a}$  to hold for either ion or electron species. To repeat, faster species are excluded from the sums. We take  $Z_{\parallel} = 1$ , which corresponds to species having the same temperature. As an example of  $Z_{\perp}$  values, a pure, single-ion species plasma has a  $Z_{\perp}$  value of 0.5.

We include appropriate modifications to the diffusion equation such as changing the denominator of operators to avoid divergent behavior and adding a source term. Zero flux is enforced at the loss-cone boundary as we consider low-collisionality mirror machines. We simulate  $K$  e-foldings of the distribution past the loss-cone vertex. That is, the simulation domain boundary is  $x_{\max} = \sqrt{\phi + K}$ . The simulation implements the finite-element method using the DolfinX library. More details of the numerical simulation set-up can be found in Ochs *et al.* (2023).

Furthermore, we choose to neglect relativistic effects. For the rest of the paper, we find it more convenient to work with the pair of coordinates  $(x, \theta)$ , where  $x$  is the dimensionless speed defined in (4.2) and  $\theta$  is pitch angle

$$\theta := \cos^{-1}(\xi). \quad (4.4)$$

We place a cold Maxwellian source  $f_s(x, \theta; T_s)$  at the origin of momentum space

$$f_s(x, \theta; T_s) = \pi^{-3/2} e^{-x^2/T_s}. \quad (4.5)$$

Here,  $T_s$  is the parameter determining the relative strength of the source's physical temperature to the steady-state system's background distribution physical temperature. The collision operator assumes a fixed hotter Maxwellian background distribution that the source particles collide with. Cold sources correspond to smaller

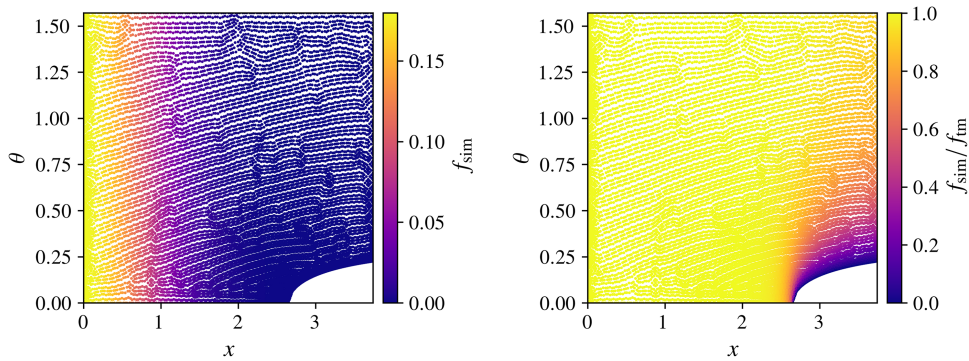


FIGURE 1. On the left, we numerically simulate  $f_{\text{sim}}(x, \theta)$  for  $\phi = 7$ ,  $R_0 = 10$ ,  $Z_{\perp} = 1$  and  $K = 7$ . The simulation is close to Maxwellian as evidenced by its near independence of  $\theta$  and exponential decay in  $x$ . On the right, we plot the weighted simulation  $g_{\text{sim}} := f_{\text{sim}}/f_{\text{tm}}$  for the same parameters.

values of  $T_s$ , which reduces the source's effect on the overall steady-state particle distribution. For the rest of the paper, we typically choose  $T_s = 0.1$  as a sufficiently small value to be considered cold.

To understand simulation-specific constraints on  $g_{\text{mod}}$ , we look at the weighted simulation  $g_{\text{sim}}$ . An example of  $f_{\text{sim}}$  and  $g_{\text{sim}}$  is shown in figure 1. Our simulations are limited to positive  $x$  and  $\theta \in [0, \pi/2]$ . We can find our prefactor expression for this region, and our constraint of cylindrical symmetry in (3.5) allows us to extend the expression to all of momentum space.

Note, in this momentum-space Fokker–Planck equation, the relative velocity of colliding particles is approximated with the velocity of the hotter, non-thermal particle. Due to this approximation and the effect of the source term, the simulated solution will somewhat worsen for  $x < 1$ , impacting the low  $\phi$  regime then. Our model is intended as a general approximation that focuses on the tail behaviors of distributions with a Maxwellian bulk, agnostic of any source terms. In the low  $\phi$  regime, the distribution is more sensitive to the specific source term, so finding any single general model is inherently challenging.

## 5. Finding our prefactor

We present a simple logarithmic prefactor to the truncated Maxwellian. To do this, we observe a useful parametrization of momentum space that reduces our problem to two dimensions. We then fit a logarithmic expression. To improve our model near the loss-cone vertex, we implement a “shift” to our parametrization and evaluate its effectiveness.

### 5.1. Parametrization by constant $R$ curves

It is convenient to simplify our problem from finding a function of two variables to one. If we can identify a parameter  $p$  that associates a value with each level curve of  $g_{\text{sim}}$  and also some independent parameter  $\eta$ , we can change our momentum-space coordinates from  $(x, \theta)$  to  $(p, \eta)$ . Our prefactor  $g_{\text{mod}}$  should only have dependence on parameter  $p$  since we want  $g_{\text{sim}}$  and  $g_{\text{mod}}$  to have the same level curves.

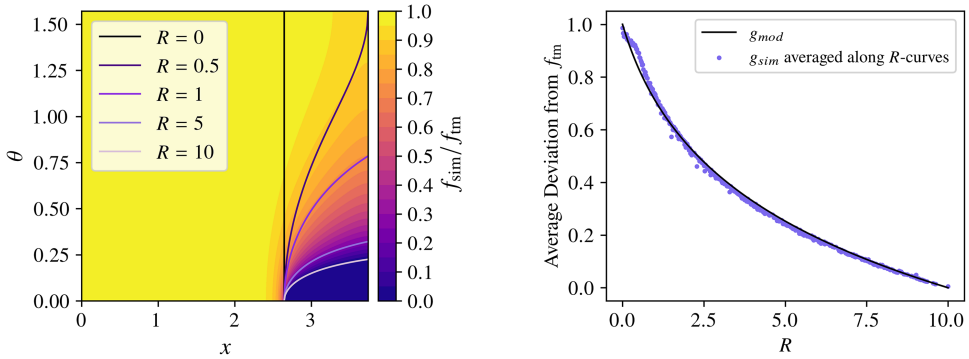


FIGURE 2. To the left, we have the  $g_{\text{sim}}$  contour plot for  $\phi = 7$  and  $R_0 = 10$ . We have added some loss-cone curves used for parametrization. To the right, we plot  $g_{\text{sim}}$  with respect to  $R$  for the same  $\phi$  and  $R_0$ . For each  $R = R_c$  value, we averaged all the  $g_{\text{sim}}$  values from points that had  $R$  values within 0.002 of  $R_c$ . Note the close fit to the overlaid proposed prefactor for high  $R$  values, which corresponds to the region around the physical loss cone.

Our intuition for a possible parametrization lies in the loss-cone condition. Setting equality and rearranging, the loss-cone boundary can be written as the following:

$$R_0 = \frac{x^2 - \phi}{x^2 \sin^2(\theta)}. \quad (5.1)$$

Let us vary  $R_0$  without changing  $\phi$ . This results in another loss-cone curve that goes through the same vertex as our physical loss cone. As shown in figure 2, we notice that there is good agreement of these effective loss-cone curves with the level curves of the weighted simulation. This motivates us to choose our independent parameter  $R$  defined as the following:

$$R(x, \theta) = \frac{x^2 - \phi}{x^2 \sin^2(\theta)}, \quad (5.2)$$

where constant- $R$  curves in momentum space closely match the level curves of the weighted simulation.

In other words, there is a physical value of  $R(x, \theta)$  that corresponds to the loss cone for the actual, physical magnetic field in the system, but it turns out that the loss-cone curves we would have had with other magnetic fields trace out curves that resemble the level sets of the distribution function. The case  $R = 0$  corresponds exactly to the vertical line through the physical loss cone's vertex while  $R = R_0$  corresponds to the physical loss cone. The range  $R \in (0, R_0)$  covers the region between the vertical line and the physical loss cone in momentum space. This  $R$  identification successfully captures an important behavior of the model, namely that the plasma diffuses more quickly across  $\theta$  than  $x$ .

## 5.2. Deviations

We analytically approximate  $g_{\text{mod}}(R; R_0, \phi)$  by examining the level curves of the weighted simulation more closely. For  $R \leq 0$ , which captures the bulk of the distribution, we expect the distribution there to be close to Maxwellian. We set our prefactor for  $R \leq 0$  to be unity. For  $R \geq R_0$ , which is the loss-cone region, the distribution must vanish there. We set our prefactor for  $R \geq R_0$  to be 0. Note, this

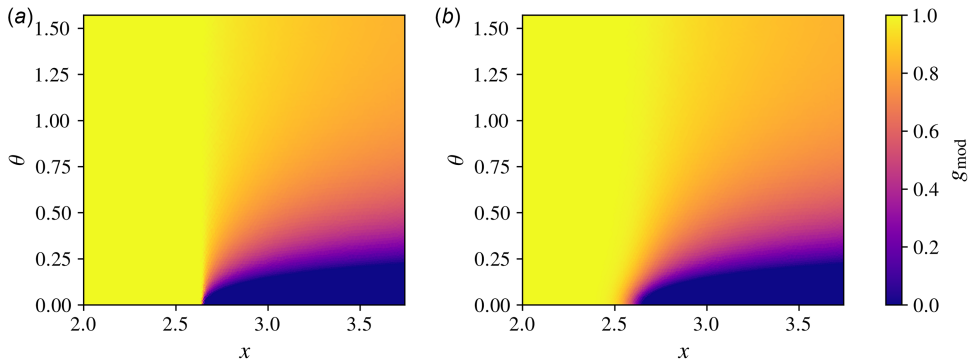


FIGURE 3. We plot  $g_{\text{mod}}$  near the loss-cone vertex for  $\phi = 7$ ,  $R_0 = 10$  and  $Z_{\perp} = 1$ . On the left, we use the unshifted parametrization which captures most of the smooth decay to the loss cone from  $g_{\text{sim}}$  in figure 1. On the right, we use the shifted parametrization, which noticeably improves the behavior at the vertex.

behavior has already been accounted for by the Heaviside theta function in the general form of  $f_{\text{mod}}$  in (3.1), but we still enforce this choice for  $R$  for consistency.

What remains is to find an analytic expression for  $g_{\text{mod}}(R; R_0, \phi)$  in the region  $R \in [0, R_0]$ . To ensure smooth decay to the loss cone, we require that this function monotonically decreases and satisfies the following boundary conditions:

$$g_{\text{mod}}(0; R_0, \phi) = 1, \quad g_{\text{mod}}(R_0; R_0, \phi) = 0. \quad (5.3)$$

Naturally, we must recast the weighted simulation to be a function of the variable  $R$ . Then,  $g_{\text{sim}}(R; R_0, \phi)$  corresponds to the average deviation of the numerical simulation from the truncated Maxwellian over the constant- $R$  curve. We find good agreement of this recast  $g_{\text{sim}}$  to a logarithmic function, which is shown in figure 2. Our complete prefactor is the following:

$$g_{\text{mod}}(R; R_0, \phi) = \begin{cases} 1 & R < 0, \\ 1 - \log_{1+R_0}(1 + R) & 0 \leq R < R_0, \\ 0 & R \geq R_0. \end{cases} \quad (5.4)$$

Overall, for a fixed  $\phi$  value, we see that the  $g_{\text{mod}}$  prefactor is a close match for most  $R$  values except at low  $R$ . An example of  $g_{\text{mod}}$  for fixed  $\phi$  and  $R_0$  is shown in figure 3.

This low- $R$  behavior stems from our assumption that all the constant- $R$  curves intersect the same vertex, which is not generally true as  $R$  goes to zero. The assumption forces an infinite gradient at the vertex, which is un-physical. When  $\phi$  is large, this is a safe assumption since the bulk of the distribution is Maxwellian and the numerical simulation's level curves appear compressed towards the vertex. However, when  $\phi$  is small, the assumption worsens as the loss cone cuts into the bulk of the distribution. The numerical simulation's level curves then appear spread out from the vertex.

### 5.3. Shifts

One way to correct the infinite gradient issue at the loss-cone vertex is by shifting the constant- $R$  curves to lie at different vertices, which are the square roots of some corresponding effective potential  $\phi_{\text{eff}}$ .

The challenge is to find some simple smooth interpolation connecting  $R$  and  $\phi_{\text{eff}}$  that satisfies the following behaviors. The original loss cone must be preserved at  $R = R_0$ . As  $R$  approaches  $R_0$ , the loss cones need to stay compressed, and  $\phi_{\text{eff}} \approx \phi$ . As  $R$  approaches 0, the loss cones need to spread out, and the shift is maximal. Lastly, as  $\phi$  goes to infinity, we should also recover the unshifted prefactor.

Let us consider the linear interpolation, where we choose to parametrize  $R \in [0, R_0]$  and  $\phi_{\text{eff}} \in [0, \phi]$  as the following:

$$R(\alpha) = \alpha R_0, \quad \phi_{\text{eff}} = \alpha \phi, \quad (5.5)$$

where  $\alpha \in [0, 1]$ . Note, the  $R = 0$  curve, which is the vertical line, is shifted to  $x = 0$ . We solve for  $R$

$$R(x, \theta) = \frac{x^2 R_0}{R_0 x^2 \sin^2 \theta + \phi}. \quad (5.6)$$

This interpolation lacks the correct limiting behavior as  $\phi$  goes to infinity, but by recursively iterating  $n$  times, we get the following interpolation:

$$R(x, \theta; n) = \frac{x^2 R(x, \theta; n-1)}{R(x, \theta; n-1) x^2 \sin^2 \theta + \phi}. \quad (5.7)$$

This recursion relation can be solved for any  $n \in \mathbb{N}$

$$R_n(x, \theta) = \frac{R_0 (\phi - x^2)}{(\phi/x^2)^n (\phi - x^2) + R_0 x^2 \sin^2(\theta) [(\phi/x^2)^n - 1]}. \quad (5.8)$$

For any  $n \in \mathbb{N}$  and  $(x, \theta)$  on the physical loss cone,  $R_n(x, \theta) = R_0$ , so the loss cone is preserved. This recursion interpolation also has the property that, for a given  $(x, \theta)$  that is not on the loss cone,  $R(x, \theta, n-1) > R(x, \theta, n)$ . Increasing  $n$  compresses the constant- $R$  curves closer to the physical loss cone. To see this, as  $n$  approaches  $\infty$ , we recover the unshifted model. Note, our prefactor case  $g_{\text{mod}} = 1$  for unshifted  $R < 0$  is equivalent to setting  $R = 0$  for the region  $x < \sqrt{\phi}$  and  $R_{n \rightarrow \infty}(x, \theta)$  indeed approaches zero for that region and also approaches our unshifted  $R$  in (5.2) for  $x > \sqrt{\phi}$ .

We can find analytic expressions for  $n$  by fitting the prefactor from shifted  $R$  to the weighted simulation for a range of  $R_0$  and  $\phi$ . Specifically, for a given  $R_0$  and  $\phi$ , we find  $n$  value that minimizes an error metric described later in (6.1). We require  $n \geq 1$  since, below one, the loss-cone shapes for low  $R$  curve towards  $x = 0$ , which is un-physical. In general, we find a nearly linear relationship between  $n$  and  $\phi$  and nearly square root dependence between  $n$  and  $R_0$ , which we then fit to the simulated best-fit  $n$  values. Below are two fits as seen in figure 4

$$n(R_0, \phi) = \left( \sqrt{1.57 R_0} + 0.93 \right) \phi + 1 \quad (Z_{\perp} = 0.5), \quad (5.9a)$$

$$n(R_0, \phi) = \left( \sqrt{1.8 R_0} + 1 \right) \phi + 1 \quad (Z_{\perp} = 1). \quad (5.9b)$$

We find that implementing some form of an interpolated shift improves the model in the low  $\phi$  regime, as seen in figure 3, but the precise form of  $n(R_0, \phi)$  does not



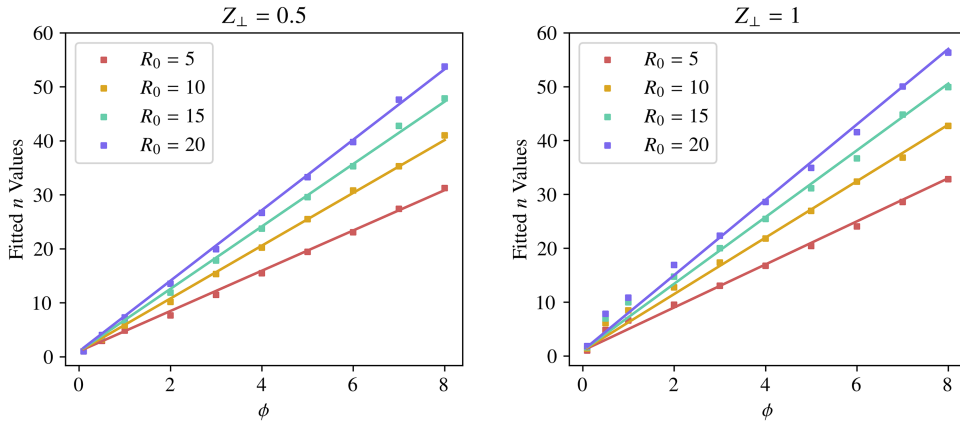


FIGURE 4. Analytic fits for the simulated best-fit  $n$  values for  $Z_{\perp} = 0.5$  on the left and  $Z_{\perp} = 1$  on the right. The fit is worse for  $\phi < 1$ , which makes sense since our model was found for  $\phi > 3$ . As  $Z_{\perp}$  decreases, the loss-cone curves should be shifted more due to decreased perpendicular diffusion. The  $n$  values should then be correspondingly smaller, especially in the low  $\phi$  region.

make much of a difference as long as  $n$  monotonically increases with respect to  $\phi$  and  $R_0$  and  $n(R_0, 0) > 1$ .

We note here that our analytic model runs approximately 30 times faster than a single run of the finite-element solver, with both using a mix of C and Python. In conjunction with its independence of simulation codes, the analytic model has a substantial computational advantage over the numerical simulations.

## 6. Error metric comparisons

In this section, we demonstrate an error comparison of analytic models with the numerical simulation. We find that the proposed model  $f_{\text{mod}}$  more closely matches the numerical simulation compared with the truncated Maxwellian model for most values of  $\phi$  and  $R_0$ . The exception is a region spiking for low  $R_0$  centered around  $\phi = 0.2$ .

We used the following error metric:

$$E(f) = \sum_{(x,\theta)} (f(x, \theta; R_0, \phi) - f_{\text{sim}}(x, \theta; R_0, \phi))^2, \quad (6.1)$$

where  $f$  is an arbitrary analytic model for the steady-state particle distribution. All points in our momentum space are weighted equally. Results for our proposed analytic, truncated Maxwellian, Najmabadi and Volosov models for fixed  $Z_{\perp} = 0.5$  are shown in figure 5. We note that the proposed model  $f_{\text{mod}}$  outperforms the truncated Maxwellian for regions of relatively good confinement,  $R_0 > 5$  and  $\phi > 2$ , as shown in figure 6. This makes sense because our model was originally fitted to this region of stronger confining potential and larger mirror ratio.

The Najmabadi model  $f_{\text{naj}}$  does modestly better at fitting to the distribution than the truncated Maxwellian around  $\phi \approx 2$ , but does significantly worse in the limit of large  $\phi$ . This is surprising since  $f_{\text{naj}}$  decays at the loss cone while the truncated Maxwellian does not. However, Najmabadi's model was developed for calculations of collisional end loss rates near the loss-cone region. As the loss-cone vertex moves

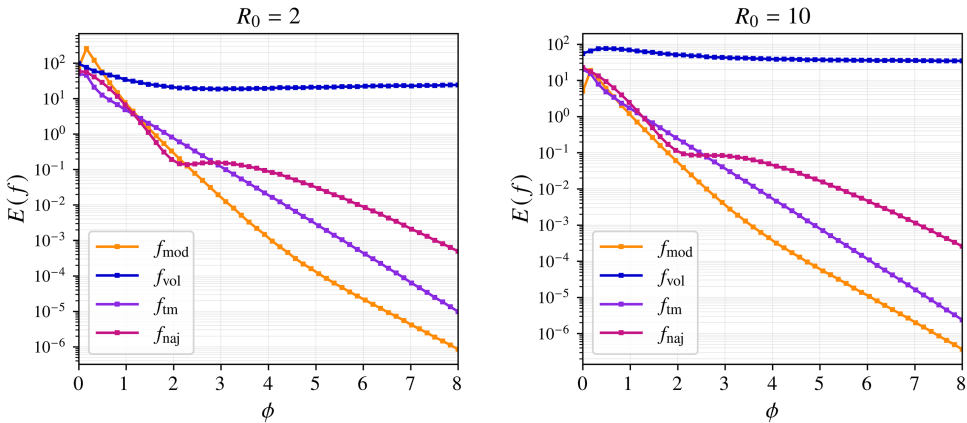


FIGURE 5. The values of  $E(f)$  of the proposed model, Volosov model, Najmabadi model and truncated Maxwellian over  $\phi \in [0, 8]$  for fixed mirror ratios. The spike at low  $\phi$  where the proposed model has greater error than the truncated Maxwellian or Najmabadi model is much less pronounced at  $R_0 = 10$  compared with  $R_0 = 2$ . For  $\phi > 3$ , the proposed model has less error by around a factor of 10 compared with the truncated Maxwellian.

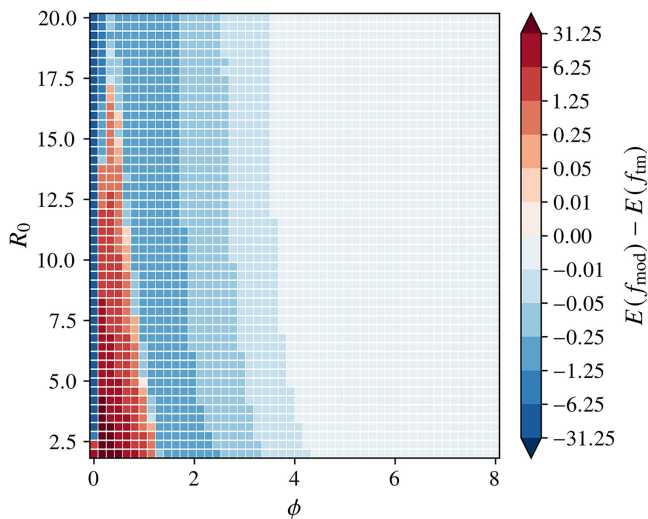


FIGURE 6. Difference of error metric results for the proposed model and the truncated Maxwellian,  $E(f_{\text{mod}}) - E(f_{\text{tm}})$ . Blue regions where the difference is negative indicate where  $f_{\text{mod}}$  outperforms  $f_{\text{tm}}$  in fitting to the numerical simulations.

further away from the bulk of the particles, fewer particles fall within the original intended region of Najmabadi's calculation. In figure 7, we see that  $f_{\text{naj}}$  overestimates the distribution in the bulk and further along the loss-cone boundary. We choose to look at the truncated Maxwellian in later analysis instead. Despite its inaccuracy at the loss cone, the truncated Maxwellian is a more consistent competitor to our model for much of parameter space. Surprisingly, the truncated Maxwellian can even outperform our proposed model in estimating the simulation at low  $\phi$  and  $R_0$ .

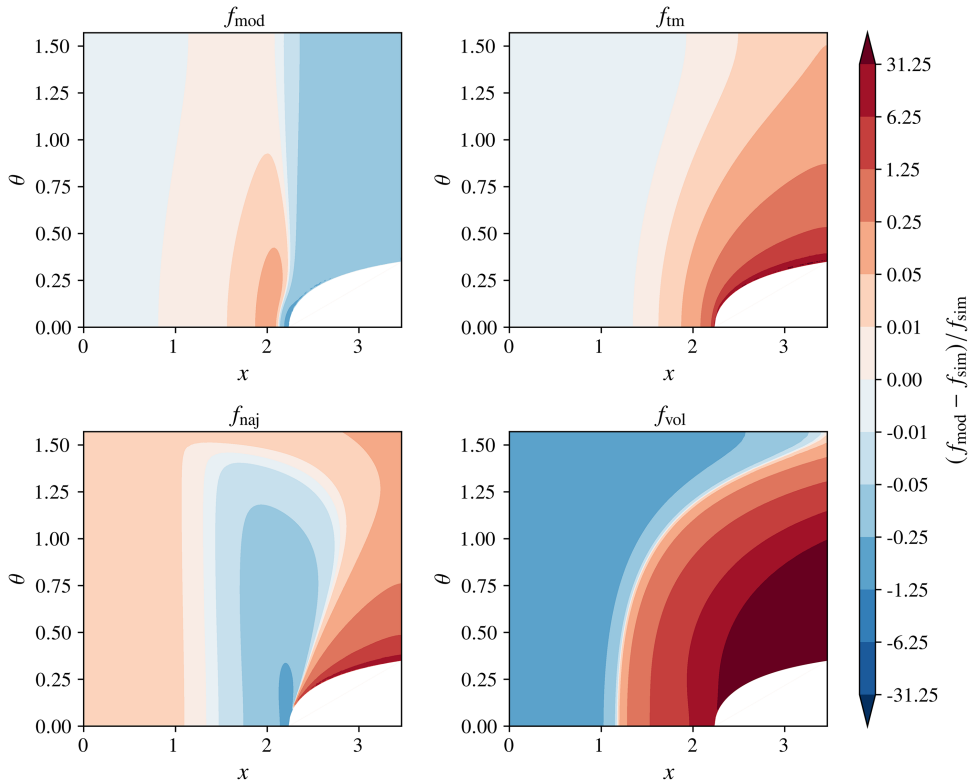


FIGURE 7. We compare the proposed, truncated Maxwellian, Najmabadi and Volosov models side by side for  $\phi = 5$  and  $R_0 = 5$  using relative error,  $(f_{\text{mod}} - f_{\text{sim}})/f_{\text{sim}}$ . Red indicates regions where the analytic model overestimates the distribution; blue, underestimates.

One possible reason for our model's worse fit at  $\phi$  close to 0 is due to the prefactor and normalization. The decay primarily impacts the tail, which is proportionally more of momentum space when  $\phi$  is small. The prefactor cuts out more of the distribution than in the simulation, leading to the normalization value to be non-trivially less than unity. However, since the value of the prefactor at low  $R$  is fixed at one, the normalization will boost values at the bulk of the distribution while preserving the model's under-prediction at the tail. This is evident in figure 8. This would also explain the narrow strip at  $\phi \approx 0$  in  $(\phi, R_0)$  parameter space where  $f_{\text{mod}}$  far outperforms the truncated Maxwellian in approximating the steady-state distribution. As  $\phi$  approaches zero, the region of low  $x$  between the origin and the vertex becomes negligible, and there are no values to be boosted.

Choosing different  $Z_{\perp} \in \{0.4, 0.6\}$  and greater source temperatures  $T_s \in \{1, 2\}$  yields roughly the same results as our choice of  $Z_{\perp} = 0.5$  and  $T_s = 0.1$ . Generally, as  $T_s$  increases or as  $Z_{\perp}$  decreases, the spiked region where our analytic model fails to outperform the truncated Maxwellian grows larger. Likewise, using the error metric that compares the weighted simulation and respective prefactors of the models led to a more definitive outperformance of our model relative to the truncated Maxwellian. The spike in  $(\phi, R_0)$  space becomes negligible. This makes sense because we had originally found our prefactor by fitting to the weighted simulation.

Due to the significant error of the Volosov model, we have omitted analysis of that model from most of the following applications. This is evident by the much

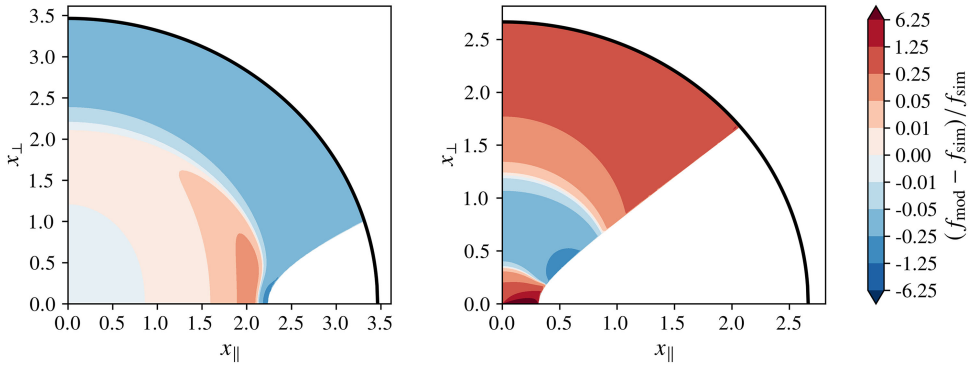


FIGURE 8. Relative error of the proposed model compared with the simulation,  $(f_{\text{mod}} - f_{\text{sim}})/f_{\text{sim}}$ . The left plot is for relatively good confinement  $\phi = 5$  and  $R_0 = 7$  while the right plot is for relatively worse confinement  $\phi = 0.1$  and  $R_0 = 2.5$ , where the proposed model is known to be worse than other analytic models. The black line marks the simulation domain.

larger error in figure 5 and the significant overestimation of the distribution at the tail in figure 7 due to the model's exponential dependence only on the perpendicular speed.

## 7. Applications

### 7.1. Stability boundary

In the limit of fast enough rotation, certain loss-cone instabilities such as the high-frequency convective loss cone (HFCLC), drift cyclotron loss cone and Dory–Guest–Harris mode can be stabilized. We are interested in the stability threshold, or minimum value of confining potential  $\phi$  for a given mirror ratio  $R_0$  that suppresses a given loss-cone mode. In this paper, we restrict ourselves to studying the HFCLC mode, comparing the predictions for the stability boundary from  $f_{\text{mod}}$  with other analytic models and numerical simulations. For more context on stability threshold problems, see Volosov *et al.* (1969), Turikov (1973) and Kolmes *et al.* (2024).

We first review the stability condition for the HFCLC mode. We define the perpendicular projected distribution as

$$\psi_a(x_\perp^2) := \bar{\psi} \int_{-\infty}^{\infty} f_a(x_\perp^2, x_\parallel^2) dx_\parallel, \quad (7.1)$$

where  $\bar{\psi}$  is the normalization constant. Note that we use the parallel and perpendicular components of momentum, not  $x$  and  $\theta$ . Perpendicular monotonicity is a sufficient condition for stabilizing the HFCLC mode

$$\frac{\partial \psi}{\partial z} \leq 0 \quad (\forall z \geq 0), \quad (7.2)$$

where  $z := x_\perp^2$ . The partial derivative with respect to  $z$  for both the truncated Maxwellian and Volosov model can be calculated analytically as done in Kolmes *et al.* (2024). However, due to the parametrization required for our analytic model, the partial derivative with respect to  $z$  for  $f_{\text{mod}}$  must be calculated numerically.

We find the stability boundaries  $\phi(R_0)$  of four distributions compared with the numerical simulations in figure 9. The stability boundary of the Volosov model can

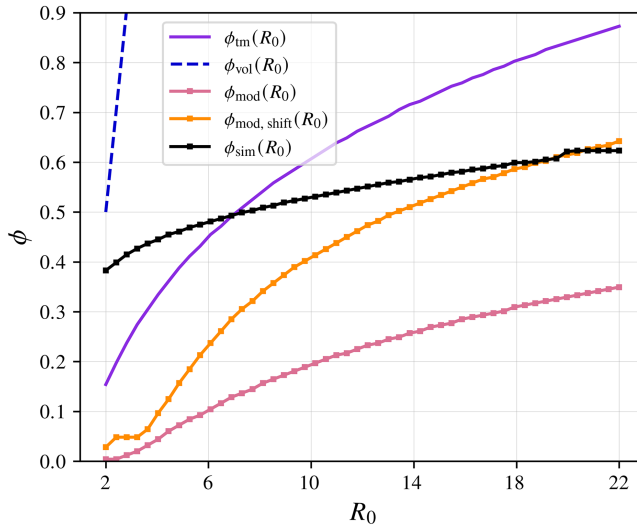


FIGURE 9. Stability boundary curves for analytic distributions and the numerical simulations.

be shown to be directly proportional to  $R_0$ , and it does not match our simulation's results. The truncated Maxwellian over-predicts the stability values for  $R_0 < 7$  and under-predicts the stability values elsewhere. As for our proposed model, we get a closer fit to the numerical simulation's stability boundary when we use the shifted as opposed to the unshifted parametrization. Both of our proposed distributions under-predict the simulation stability value, but shifting lifts the stability values of the model with unshifted parametrization.

This can be explained by understanding the region in  $(\phi, R_0)$  space where the truncated Maxwellian outperforms  $f_{\text{mod}}$  in our error analysis. The stability values are precisely at low  $\phi < 1$  values, where our model over-predicts at low  $x$  and under-predicts at higher  $x$ . This tendency of over and under estimation is visible in figure 8, which is with respect to  $x_{\parallel} - x_{\perp}$  coordinates. The cumulative effect is to boost the projected distribution at low  $z$ , enough to satisfy the perpendicular monotonicity condition when the numerical simulation does not. Increasing the mirror ratio  $R_0$  improves the performance of the model compared with the truncated Maxwellian, which is what we observe in the stability boundary curves.

## 7.2. Fusion yield

One use of analytic distribution functions is the ability to more quickly calculate fusion yields. Since fusion yield is sensitive to the tail of the distribution, the accuracy of a model in capturing behavior near the loss cone and further away from the bulk of the distribution matters more. We compare the fusion yield of the deuterium–deuterium reaction from the numerical simulation with various analytic models. We find that proposed model more closely estimates the fusion yield compared with the truncated Maxwellian. However, the model consistently underestimates fusion yield as a result of over-suppressing values at the loss cone. For further context on fusion yield problems, see the following: Kalra, Agrawal & Pandimani (1988), Nath, Majumdar & Kalra (2013), Kolmes, Mlodik & Fisch (2021), Xie *et al.* (2023), Kong *et al.* (2024) and Fetsch & Fisch (2025).

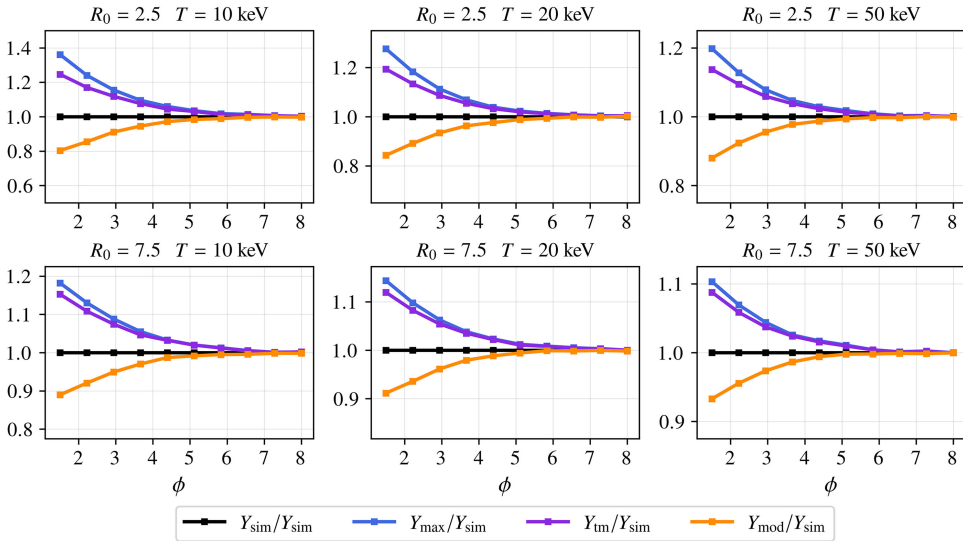


FIGURE 10. We plot relative fusion yields  $Y_f/Y_{\text{sim}}$  for fixed temperatures and mirror ratios. We vary confining potentials  $\phi \in [1, 8]$ . Note, as  $\phi$  increases, all the models converge to the simulation results as they all look essentially Maxwellian in this limit.

To find fusion yield, the fusion reaction rate  $Y$  between two ion species can be expressed as the following integral expression:

$$Y(f_a, f_b) = \int d^3 \mathbf{v}_a d^3 \mathbf{v}_b \sigma(w) w f_a(\mathbf{v}_a) f_b(\mathbf{v}_b), \quad (7.3)$$

where  $w := |\mathbf{v}_a - \mathbf{v}_b|$  is relative speed,  $f_a$  and  $f_b$  are the distribution functions of the ion species and  $\sigma$  is the respective cross-section between species  $a$  and  $b$ . This six-dimensional integral can be reduced to a five-dimensional integral by using cylindrical symmetry for one of the ion species. To numerically evaluate the fusion yield integral, we use the VEGAS Monte Carlo algorithm as described in Lepage (1978).

For simplicity, we find the reaction rate of a single-ion species, deuterium, for the deuterium–deuterium reaction at temperatures 10, 20 and 50 keV for different mirror ratios and confining potentials. The ion species then has  $Z_\perp$  value of 0.5 exactly. We find the fusion yields of three models, the Maxwellian, truncated Maxwellian and our proposed model as well as the fusion yield of the numerical steady-state simulation. Our yield calculations are shown in figure 10 for varying confining potential, and figure 11 for varying mirror ratios.

When ranging over both confining potentials and mirror ratios, we find that the proposed model has less relative error compared with the truncated Maxwellian. We first note that the model under-predicts the fusion yield while the truncated Maxwellian over-predicts. The reason can be found in the tail behavior. The Maxwellian slightly over-predicts compared with the truncated Maxwellian, with the only difference between the distributions being the removal of the loss-cone particles and resultant change in normalization constant. From figure 8, since we are considering relatively good confinement with  $\phi > 1$  and  $R_0 \geq 2$ , it is evident that



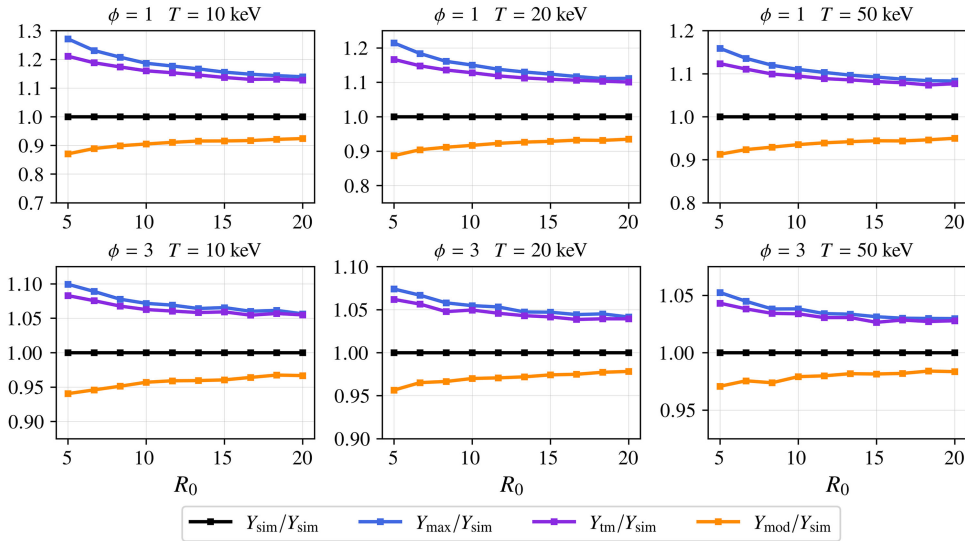


FIGURE 11. We plot relative fusion yields  $Y_f/Y_{\text{sim}}$  for fixed temperatures and confining potentials. We vary mirror ratios  $R_0 \in [5, 20]$ . The model better predicts fusion yield compared with the Maxwellian and truncated Maxwellian for all mirror ratios.

our model over-suppresses the distribution values at the tail, leading to a consistent under-prediction of fusion yield.

### 7.3. Free energy

Finally, we consider the calculation of free energy associated with the steady-state particle distribution. Free (or available) energy is the maximum amount of energy extractable from a given initial distribution after specifying rules on allowed phase-space rearrangements. Equivalently, free energy also provides a bound on the amount of energy that can go into instabilities before reaching a distribution called the ground state, which is necessarily stable. If a relation can be found between available energy and another stability-related quantity, available energy could serve as a computationally simpler proxy measurement for that other quantity, as demonstrated for turbulent energy flux in tokamaks and stellarators (Mackebach, Proll & Helander 2022, 2023a, b). We study the free energy of the proposed model, truncated Maxwellian and numerical simulation subject to two different sets of rearrangement constraints.

We briefly review necessary background on free energy and relevant constraints. Free energy subject to the sole constraint that all rearrangements must preserve phase-space volumes is called the Gardner free energy (Gardner 1963). Reaching a ground state is equivalent to rearranging the initial velocity-space distribution into a distribution  $f$  that is monotonically decreasing with respect to energy. The energy of a distribution is commonly chosen as the total kinetic energy  $W$ . The available energy is then calculated as the difference of the initial state's kinetic energy and the ground state's kinetic energy. However, in constructing a coarse-grained model of the distribution function that averages over some scale, we often perceive diffusion, or phase mixing. Free energy subject to the constraint that rearrangements average the densities of phase-space volumes is called diffusive free energy (Fisch & Rax 1993). Although diffusive free energy is more appropriate for the collisional diffusion behind our model, it is sufficient to calculate the Gardner free energy since it has

been shown that the two free energies are arbitrarily close in the continuous limit (Kolmes & Fisch 2020). When we refer to the unconstrained free energy, we are referring to the Gardner free energy.

Conservation of phase-space volume is often not a sufficient description of the allowed phase-space rearrangements of the plasma for any arbitrary mode. It is possible to impose additional constraints on allowed rearrangements such as the conservation of adiabatic invariants (Helander 2017, 2020). An important class of loss-cone instabilities are flute-like modes, such as the HFCLC mode, whose wavenumbers  $k$  vanish in the direction of the magnetic field. One additional constraint for these modes is that only the projected distributions corresponding to a specific  $x_\perp$  value,

$$f_P(x_\perp) = \int_{-\infty}^{\infty} f(x_\parallel, x_\perp) dx_\parallel, \quad (7.4)$$

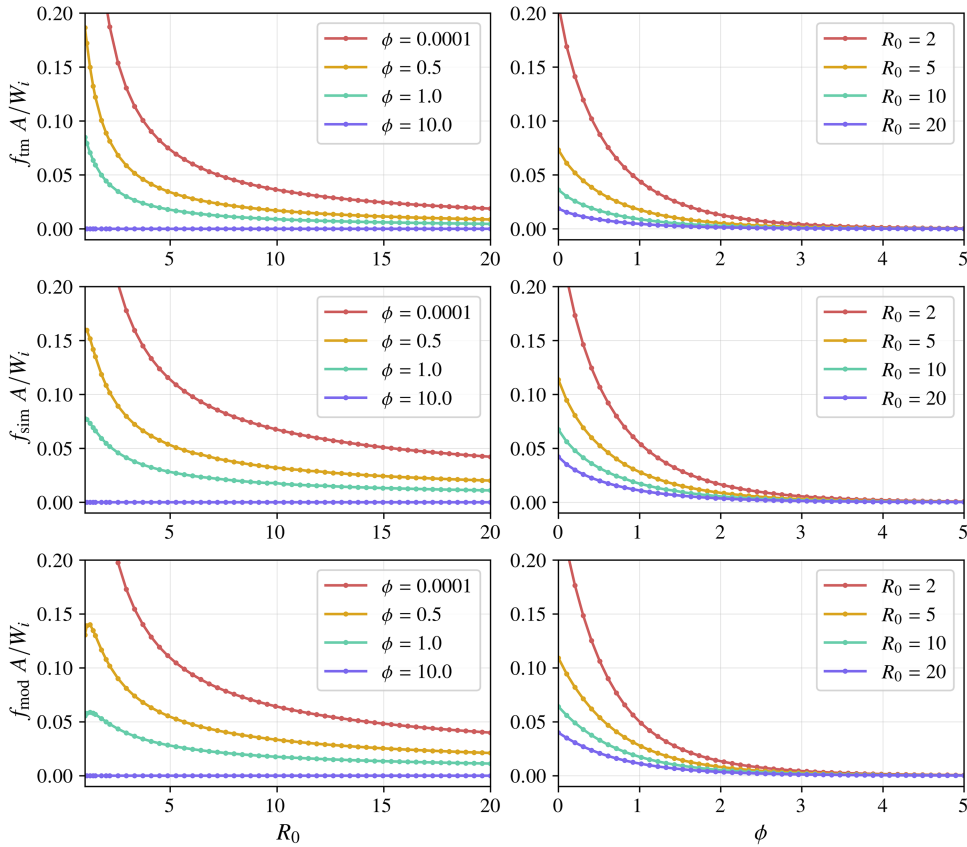
can be swapped with one another (Kolmes *et al.* 2024). This comes from the fact that the quasilinear diffusion operator cannot differentiate between phase-space elements of the same  $x_\parallel$ . When we refer to constrained free energy, we are referring to the available energy subject to both constraints of phase-space volume conservation and this flute-like loss-cone constraint. For a more extensive discussion of calculating available energy, see Kolmes, Helander & Fisch (2020) and Helander (2017, 2020).

To compare the free energy of different initial distributions, we are interested in the accessible energy fraction, or the ratio of free energy  $A$  to the total initial energy  $W_i$ . For our numerical calculations, we simulate more of velocity space by setting  $K = 12$ . We also choose a smaller source temperature  $T_s = 0.01$  so that the source does not disturb the steady-state distribution for almost negligible confining potentials.

For unconstrained free energy, the left column of figure 12 shows the accessible energy fraction's dependency on mirror ratio  $R_0$  for initial distributions for fixed confining potentials. When  $\phi = 10$ , all the distributions have zero available energy, which is what we expect. For large  $\phi$ , the loss cone moves further away from the bulk of the distribution, and thus, the initial distribution approaches the Maxwellian, which is monotonically decreasing in energy. The  $A/W_i$  values of  $f_{\text{mod}}$  closely match those of the numerical simulation for  $R_0 > 2.5$ , even for low  $\phi$  values, and outperforms the truncated Maxwellian in the  $A/W_i$  calculations. However, for low  $R_0$  values,  $f_{\text{mod}}$  underestimates  $A/W_i$  and exhibits a non-monotonic behavior close to  $R = 1$ . Our model was optimized for the  $R_0 > 5$  regime, so it makes sense for it to do poorly at low  $R_0$ .

The right column of figure 12 shows the accessible energy fraction's dependency on confining potential  $\phi$  for different initial distributions for fixed mirror ratios. The  $f_{\text{mod}}$  curves seem to closely match the numerical simulation  $A/W_i$  curves for all  $R_0$  and  $\phi$ . Meanwhile, the truncated Maxwellian underestimates  $A/W_i$  in the low  $\phi$  limit and decays faster than the numerical simulation.

For constrained free energy, the left column of figure 13 shows the accessible energy fraction's dependency on mirror ratio  $R_0$  for initial distributions with the additional flute-like mode constraint. The chosen fixed confining potentials are smaller than the unconstrained counterparts. In the low  $\phi$  limit, both the truncated Maxwellian and  $f_{\text{mod}}$  find zero available energy. In cutting out values near the loss cone, the prefactor of  $f_{\text{mod}}$  boosts values for  $x_\parallel \approx 0$  and low  $x_\perp$ , which can force the initial projected distribution to be monotonically decreasing with respect to  $x_\perp$ . The truncated Maxwellian gets closer to the immediate shape of the numerical simulation's accessible energy fraction curves. In the high  $\phi$  limit, the calculated available

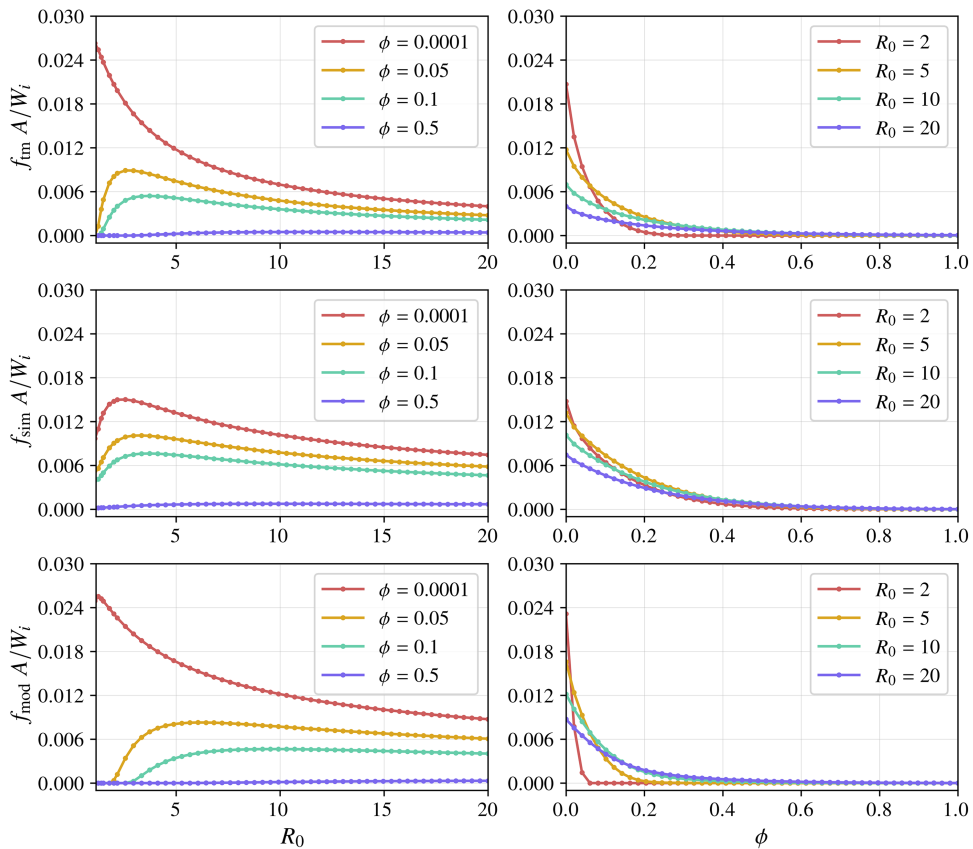
FIGURE 12. Accessible energy fraction  $A/W_i$  for the unconstrained case.

energy of  $f_{\text{mod}}$  approaches the numerical simulation's available energy values while the truncated Maxwellian underestimates.

The right column of figure 13 shows the accessible energy fraction's dependency on confining potential  $\phi$  for different initial distributions with the flute-like mode constraint. The chosen fixed mirror ratios are the same as the unconstrained case. The model  $f_{\text{mod}}$  appears to overestimate  $A/W_i$  and then decay more quickly than the numerical simulation while the truncated Maxwellian underestimates  $A/W_i$  (except for  $R_0 = 2$ ) while decaying closer to the rate that the numerical simulation does.

## 8. Discussion

In this paper, we have presented a closed-form analytic model of the steady-state particle distribution function for low-collisionality mirror traps like tandem or centrifugal traps subject to arbitrary confining potentials. The proposed distribution has the following desired qualities: (i) recovering the Maxwellian in the limit that the confining potential goes to infinity, (ii) smoothly decaying to zero at the loss-cone boundary, (iii) diffusing more rapidly in pitch angle than speed and (iv) maintaining cylindrical symmetry. Motivated by the level curves similarity to loss-cone shapes, we formulate both an 'unshifted' and 'shifted' parametrization for the model. Although the shifted formulation requires an extra parameter depending on the  $Z_{\perp}$  value, a simple approximation suffices, and we provide two such fits. Otherwise, our

FIGURE 13. Accessible energy fraction  $A/W_i$  for the constrained case.

analytic model is written explicitly below and remains flexible enough to be modified for different uses

$$f_{\text{mod}}(x, \theta; R_0, \phi) = A \left[ g_{\text{mod}}(x, \theta; R_0, \phi) \left( \pi^{-3/2} e^{-x^2} \right) \right] \Theta(\phi + R_0 x^2 \sin^2(\theta) - x^2), \quad (8.1)$$

$$g_{\text{mod}}(R; R_0, \phi) = \begin{cases} 1 & R < 0, \\ 1 - \log_{1+R_0}(1+R) & 0 \leq R < R_0, \\ 0 & R \geq R_0, \end{cases} \quad (8.2)$$

$$R(x, \theta) = \frac{x^2 - \phi}{x^2 \sin^2(\theta)} \quad (\text{unshifted}), \quad (8.3)$$

$$R_n(x, \theta) = \frac{R_0(\phi - x^2)}{(\phi/x^2)^n(\phi - x^2) + R_0 x^2 \sin^2(\theta) [(\phi/x^2)^n - 1]} \quad (\text{shifted}), \quad (8.4)$$

where fits for  $n$  are provided for  $Z_{\perp} = 0.5$  and  $Z_{\perp} = 1$  in (5.9).

We then compared several analytic models with the numerical steady-state simulated distribution with an error metric. We find that our model has nearly a factor

of 10 less of error compared with the truncated Maxwellian for mirror ratio  $R_0 > 5$  and confining potential  $\phi > 2$ . In this region of relatively good confinement, our model tends to underestimate the distribution values for larger values of momentum and more severely at the loss-cone vertex. In general, our model does better in approximating the distribution than the truncated Maxwellian except for the spike at  $\phi = 0.2$  in  $(R_0, \phi)$  space. We have also compared the truncated Maxwellian with other models and found that it performs better than expected despite un-physical behavior at the loss cone. The truncated Maxwellian is a simpler alternative to our model that has the trade-off of somewhat worse performance for much of parameter space. Note, this model is better suited for bulk-behavior applications. The truncated Maxwellian is consistently worse than our model for tail-specific applications such as fusion yield.

These analytic functions are often useful heuristic devices for studying the stability of loss-cone modes and tail behaviors. We have explored three applications for our model: the HFCLC stability boundary calculation, fusion yield for different temperatures of a deuterium-deuterium plasma and both unconstrained and constrained (by a flute-like loss-cone mode) available energy. There are a few key trends, which we review here. For the low  $\phi \ll 1$  regime, our model boosts the distribution values at low momentum, which causes a noticeable under-prediction of the minimum stability value and available energy in the constrained case. For the region of relatively good confinement, our model over-suppresses the distribution values at high momentum, in particular at the loss-cone boundary. Specifically, this behavior results in under-prediction of fusion yields, which are sensitive to the higher energy particles at the tail. Note, for relatively good confinement or sufficiently high mirror ratios for small confining potentials, our model will often more closely recover the limiting behavior of the numerical simulation compared with the truncated Maxwellian model.

It can be anticipated that improvements to our model functions can be made by refining the shift. The shift was based off a recursive linear interpolation, but other interpolations (polynomial, logarithmic, etc.) between  $R$  and  $\phi_{\text{eff}}$  are options. By either using another interpolation or finding a closed-form expression for the  $n$  parameter that accounts for different  $Z_{\perp}$  values, a further simplified expression for the model could be found that does not compromise the fit of the model to the numerical simulations.

Our analytic distribution can also be used to calculate radiation loss quantities in rotating mirrors to judge the viability of the configuration (Mlodik *et al.* 2023; Munirov & Fisch 2023; Ochs, Mlodik & Fisch 2024). Additionally, the yield calculation shown in § 7.2 could be extended to calculate the birth distribution of fusion products in phase space, which is important for alpha-extraction problems (Fisch & Rax 1992; Mynick & Pomohrey 1994; Fisch 2006; Zhmoginov & Fisch 2008; Bierwage *et al.* 2022; Gudinetsky *et al.* 2025). Comparisons between the proposed model and numerical simulations could then be made with respect to these calculations to judge the accuracy of our model. Improving upon these heuristic models is essential to better understanding and more quickly calculating quantities of interest in centrifugal and tandem mirrors.

### Acknowledgements

The authors would like to thank M. Rosen, T. Rubin, and A. Glasser for helpful conversations.

*Editor Cary Forest thanks the referees for their advice in evaluating this article.*

## Funding

This research was performed with support from the Program in Plasma Science and Technology (PPST), under US DOE contract number DE-AC02-09CH11466. G.L. was supported by Princeton University's Office of Undergraduate Research Undergraduate Fund for Academic Conferences through the Hewlett Foundation Fund. This work was also supported by APRA-E Grant No. DE-AR0001554.

## Declaration of interests

The authors report no conflict of interest.

## REFERENCES

- ABDRASHITOV, G.F., BELOBORODOV, A.V., VOLOSOV, V.I., KUBAREV, V.V., POPOV, Y.S. & YUDIN, Y.N. 1991 Hot rotating plasma in the PSP-2 experiment. *Nucl. Fusion* **31**, 1275.
- BEKHTENEV, A.A., VOLOSOV, V.I., PAL'CHIKOV, V.E., PEKKER, M.S. & YUDIN, Y.N. 1980 Problems of a thermonuclear reactor with a rotating plasma. *Nucl. Fusion* **20**, 579.
- BE'ERY, I., GERTSMAN, A. & SEEMAN, O. 2018 Plasma confinement by moving multiple mirrors. *Plasma Phys. Control Fusion* **60**, 115004.
- BIERWAGE, A., *et al.* 2022 Energy-selective confinement of fusion-born alpha particles during internal relaxations in a tokamak plasma. *Nat. Commun.* **13**, 3941.
- CATTO, P.J. & BERNSTEIN, I.B. 1981 Collisional end losses from conventional and tandem mirrors. *Phys. Fluids* **24**, 1900–1905.
- CATTO, P.J. & LI, X.Z. 1985 Particle loss rates from electrostatic wells of arbitrary mirror ratios. *Phys. Fluids* **28**, 352–357.
- CHO, T., *et al.* Observation of the effects of radially sheared electric fields on the suppression of turbulent vortex structures and the associated transverse loss in GAMMA 10. *Phys. Rev. Lett.* **94**, 085002.
- DOLGOLENKO, D.A. & MUROMKIN, Y.A. 2017 Separation of mixtures of chemical elements in plasma. *Phys.-Usp.* **60**, 994.
- EGEDAL, J., ENDRIZZI, D., FOREST, C.B. & FOWLER, T.K. 2022 Fusion by beam ions in a low collisionality, high mirror ratio magnetic mirror. *Nucl. Fusion* **62**, 126053.
- ELLIS, R.F., CASE, A., ELTON, R., GHOSH, J., GRIEM, H., HASSAM, A., LUNSFORD, R., MESSER, S. & TEODORESCU, C. 2005 Steady supersonically rotating plasmas in the Maryland Centrifugal Experiment. *Phys. Plasmas* **12**, 055704.
- ELLIS, R.F., HASSAM, A.B., MESSER, S. & OSBORN, B.R. 2001 An experiment to test centrifugal confinement for fusion. *Phys. Plasmas* **8**, 2057.
- FETSCH, H. & FISCH, N.J. 2025 Enhancement to fusion reactivity in sheared flows. arXiv: 2410.03590.
- FETTERMAN, A.J. & FISCH, N.J. 2011 Metrics for comparing plasma mass filters. *Phys. Plasmas* **18**, 103503.
- FISCH, N.J. 2006 Alpha channeling in mirror machines. *Phys. Rev. Lett.* **97**, 225001.
- FISCH, N.J. & RAX, J.-M. 1992 Interaction of energetic alpha particles with intense lower hybrid waves. *Phys. Rev. Lett.* **69**, 612.
- FISCH, N.J. & RAX, J.-M. 1993 Free energy in plasmas under wave-induced diffusion. *Phys. Fluids B* **5**, 1754.
- FUTCH, A.H., Jr., HOLDREN, J.P., KILLEEN, J. & MIRIN, A.A. 1972 Multi-species fokker-planck calculations for d-t and d-3he mirror reactors. *Plasma Phys.* **14**, 211.
- GARDNER, C.S. 1963 Bound on the energy available from a plasma. *Phys. Fluids* **6**, 839.
- GUDINETSKY, E., MILLER, T., BE'ERY, I. & Barth Ido 2025 Autoresonant removal of fusion products in mirror machines. *Phys. Rev. Lett.* **134**, 155101.
- GUEROULT, R. & FISCH, N.J. 2014 Plasma mass filtering for separation of actinides from lanthanides. *Plasma Sour. Sci. Technol.* **23**, 035002.
- GUEROULT, R., HOBBS, D.T. & FISCH, N.J. 2015 Plasma filtering techniques for nuclear waste remediation. *J. Hazard. Mater.* **297**, 153–159.
- GUEROULT, R., RAX, J.-M. & FISCH, N.J. 2014 The double well mass filter. *Phys. Plasmas* **21**, 020701.



- GUEROULT, R., RAX, J.-M. & FISCH, N.J. 2018 Opportunities for plasma separation techniques in rare earth elements recycling. *J. Clean. Prod.* **182**, 1060–1069.
- HELANDER, P. 2017 Available energy and ground states of collisionless plasmas. *J. Plasma Phys.* **83**, 715830401.
- HELANDER, P. 2020 Available energy of magnetically confined plasmas. *J. Plasma Phys.* **86**, 905860201.
- HIDEKUMA, S., HIROE, S., WATARI, T., SHOJI, T., SATO, T. & TAKAYAMA, K. 1974 Preferential radiofrequency plugging of multi-ion species plasmas in a static cusped confinement system. *Phys. Rev. Lett.* **33**, 1537–1540.
- HIROE, S., HIDEKUMA, S., WATARI, T., SHOJI, T., SATO, T. & TAKAYAMA, K. 1975 Radio-frequency preferential plugging of multi-ion-species plasma in cusped magnetic devices. *Nucl. Fusion* **15**, 769.
- IVANOV, A.A. & PRIKHODKO, V.V. 2013 Gas-dynamic trap: an overview of the concept and experimental results. *Plasma Phys. Control Fusion* **55**, 063001.
- IVANOV, A.A. & PRIKHODKO, V.V. 2017 Gas dynamic trap: experimental results and future prospects. *Phys. Usp.* **60**, 509–533.
- KALRA, M.S., AGRAWAL, S. & PANDIMANI, S. 1988 Fusion reactivities for non-Maxwellian ion velocity distributions. *Trans. Amer. Nucl. Soc.* **56**, 126.
- KHUDIK, V.N. 1997 Longitudinal losses of electrostatically confined particles from a mirror device with arbitrary mirror ratio. *Nucl. Fusion* **37**, 189–198.
- KOLMES, E.J. & FISCH, N.J. 2020 Recovering Gardner restacking with purely diffusive operations. *Phys. Rev. E* **102**, 063209.
- KOLMES, E.J. & FISCH, N.J. 2024 Upper and lower bounds on phase-space rearrangements. *Phys. Plasmas* **31**, 042109.
- KOLMES, E.J., HELANDER, P. & FISCH, N.J. 2020 Available energy from diffusive and reversible phase space rearrangements. *Phys. Plasmas* **27**, 062110.
- KOLMES, E.J., MLODIK, M.E. & FISCH, N.J. 2021 Fusion yield of plasma with velocity-space anisotropy at constant energy. *Phys. Plasmas* **28**, 052107.
- KOLMES, E.J., OCHS, I.E. & FISCH, N.J. 2024 Loss-cone stabilization in rotating mirrors: thresholds and thermodynamics. *J. Plasma Phys.* **90**, 905900203.
- KONG, H., XIE, H., LIU, B., TAN, M., LUO, D., LI, Z. & SUN, J. 2024 Enhancement of fusion reactivity under non-Maxwellian distributions: effects of drift-ring-beam, slowing-down, and kappa superthermal distributions. *Plasma Phys. Control Fusion* **66**, 015009.
- LEHNERT, B. 1971 Rotating plasmas. *Nucl. Fusion* **11**, 485.
- LEPAGE, G.P. 1978 A new algorithm for adaptive multidimensional integration. *J. Comput. Phys.* **27**, 192.
- LITVAK, A., AGNEW, S., ANDEREGG, F., CLUGGISH, B., FREEMAN, R., GILLELAND, J., ISLER, R., LEE, W., MILLER, R. & OHKAWA, T. 2003 Archimedes plasma mass filter. In *30th EPS Conference on Control Fusion and Plasma Physics*, vol. 27.
- MACKENBACH, R.J.J., PROLL, J.H.E. & HELANDER, P. 2022 Available energy of trapped electrons and its relation to turbulent transport. *Phys. Rev. Lett.* **128**, 175001.
- MACKENBACH, R.J.J., PROLL, J.H.E., SNOEP, G. & HELANDER, P. 2023a Available energy of trapped electrons in Miller tokamak equilibria. *J. Plasma Phys.* **89**, 905890522.
- MACKENBACH, R.J.J., PROLL, J.H.E., WAKELKAMP, R. & HELANDER, P. 2023b The available energy of trapped electrons: a nonlinear measure for turbulent transport. *J. Plasma Phys.* **89**, 905890513.
- MILLER, T., BE'ERY, I. & Barth Ido 2021 Rate equations model for multiple magnetic mirrors in various thermodynamic scenarios. *Phys. Plasmas* **28**, 112506.
- MLODIK, M.E., MUNIROV, V.R., RUBIN, T. & FISCH, N.J. 2023 Sensitivity of synchrotron radiation to the superthermal electron population in mildly relativistic plasma. *Phys. Plasmas* **30**, 043301.
- MUNIROV, V.R. & FISCH, N.J. 2023 Suppression of bremsstrahlung losses from relativistic plasma with energy cutoff. *Phys. Rev. E* **107**, 065205.
- MYNICK, H.E. & POMOHREY, N. 1994 Frequency sweeping: a new technique for energy-selective transport. *Nucl. Fusion* **34**, 1277.
- NAJMABADI, F., CONN, R.W. & COHEN, R.H. 1984 Collisional end loss of electrostatically confined particles in a magnetic mirror field. *Nucl. Fusion* **24**, 75.
- NATH, D., MAJUMDAR, R. & KALRA, M.S. 2013 Thermonuclear fusion reactivities for drifting tri-Maxwellian ion velocity distributions. *J. Fusion Energy* **32**, 457.

- NEWCOMB, W.A. 1981 Equilibrium and stability of collisionless systems in the paraxial limit. *J. Plasma Phys.* **26**, 529.
- OCHS, I.E., MLODIK, M.E. & FISCH, N.J. 2024 Electron tail suppression and effective collisionality due to synchrotron emission and absorption in mildly relativistic plasmas. *Phys. Plasmas* **31**, 083303.
- OCHS, I.E., MUNIROV, V.R. & FISCH, N.J. 2023 Confinement time and ambipolar potential in a relativistic mirror-confined plasma. *Phys. Plasmas* **30**, 052508.
- OHKAWA, T. & MILLER, R.L. 2002 Band gap ion mass filter. *Phys. Plasmas* **9**, 5116–5120.
- OILER, A.P., USMANOV, R.A., ANTONOV, N.N., GAVRIKOV, A.V. & SMIRNOV, V.P. 2024 Increasing the efficiency of plasma mass separation by optimizing the electric potential. *Plasma Phys. Rep.* **50**, 588–596.
- POST, R.F. 1987 The magnetic mirror approach to fusion. *Nucl. Fusion* **27**, 1579.
- POST, R.F. & ROSENBLUTH, M.N. 1966 Electrostatic instabilities in finite mirror-confined plasmas. *Phys. Fluids* **9**, 730.
- ROSEN, M.H., SENGUPTA, W., OCHS, I., PARRA, F.I. & HAMMETT, G.W. 2025 Enhanced collisional losses from a magnetic mirror using the Lenard–Bernstein collision operator. *J. Plasma Phys.* 1–24.
- ROSENBLUTH, M.N. & POST, R.F. 1965 High-frequency electrostatic plasma instability inherent to “loss-cone” particle distributions. *Phys. Fluids* **8**, 547.
- SMITH, G.R. 1984 Alfvén ion-cyclotron instability in tandem-mirror plasmas. I. *Phys. Fluids* **27**, 1499–1513.
- SMITH, G.R., NEVINS, W.M.C. & SHARP, W.M. 1984 Alfvén ion-cyclotron instability in tandem-mirror plasmas. II. *Phys. Fluids* **27**, 2120–2128.
- SUDNIKOV, A.V., BEKLEMISHEV, A.D., POSTUPAEV, V.V., BURDAKOV, A.V., IVANOV, I.A., VASILYEVA, N.G., KUKLIN, K.N. & SIDOROV, E.N. 2017 SMOLA device for helical mirror concept exploration. *Fusion Eng. Des.* **122**, 846.
- SUMMERS, D. & STONE, S. 2025 The subtracted-kappa distribution and its properties. *Phys. Plasmas* **32**, 012112.
- TANG, W.M., PEARLSTEIN, L.D. & BERK, H.L. 1972 Finite beta stabilization of the drift-cone instability. *Phys. Fluids* **15**, 1153–1155.
- TEODORESCU, C., YOUNG, W.C., SWAN, G.W.S., ELLIS, R.F., HASSAM, A.B. & ROMERO-TALAMAS, C.A. 2010 Confinement of plasma along shaped open magnetic fields from the centrifugal force of supersonic plasma rotation. *Phys. Rev. Lett.* **105**, 085003.
- TIMOFEEV, A.V. 2014 On the theory of plasma processing of spent nuclear fuel. *Phys-USP* **57**, 990.
- TURIKOV, V.A. 1973 Effect of electric drift on the loss-cone plasma instability. *Sov. Phys. – Tech. Phys.* **18**, 48.
- VOLOSOV, V.I., PAL’CHIKOV, V.E. & TSEL’NIK, F.A. 1969 Some characteristics of rotating plasma behavior in a magnetic trap. *Sov. Phys. – Dokl.* **13**, 691.
- VORONA, N.A., GAVRIKOV, A.V., SAMOKHIN, A.A., SMIRNOV, V.P. & KHOMYAKOV, Y.S. 2015 On the possibility of reprocessing spent nuclear fuel and radioactive waste by plasma methods. *Phys. Atom. Nucl.* **78**, 1624–1630.
- WEIBEL, E.S. 1980 Separation of isotopes. *Phys. Rev. Lett.* **44**, 377–379.
- WHITE, R., HASSAM, A. & BRIZARD, A. 2018 Centrifugal particle confinement in mirror geometry. *Phys. Plasmas* **25**, 012514.
- XIE, H., TAN, M., LUO, D., LI, Z. & LIU, B. 2023 Fusion reactivities with drift bi-maxwellian ion velocity distributions. *Plasma Phys. Control Fusion* **65**, 055019.
- ZHMOGINOV, A.I. & FISCH, N.J. 2008 Simulation of  $\alpha$ -channeling in mirror machines. *Phys. Plasmas* **15**, 042506.